Effects of nucleation at a first-order transition between two superconducting phases: Application to $CeRh_2As_2$

András L. Szabó [1], Mark H. Fischer [2], and Manfred Sigrist [1]
[1]*Institute for Theoretical Physics, ETH Zurich, 8093 Zurich, Switzerland*
[2]*Department of Physics, University of Zurich, 8057 Zurich, Switzerland*

(Received 25 September 2023; revised 18 March 2024; accepted 21 March 2024; published 22 April 2024)

Recent experiments observed a phase transition within the superconducting regime of the heavy-fermion system $CeRh_2As_2$ when subjected to a c-axis magnetic field. This phase transition has been interpreted as a parity switching from even to odd parity as the field is increased, and is believed to be of first order. If correct, this scenario provides a unique opportunity to study the phenomenon of local nucleation around inhomogeneities in a superconducting context. Here, we study such nucleation in the form of sharp domain walls emerging on a background of spatially varying material properties and hence, critical magnetic field. To this end, we construct a spatially inhomogeneous Ginzburg-Landau functional and apply numerical minimization to demonstrate the existence of localized domain-wall solutions and study their physical properties. Furthermore, we propose ultrasound attenuation as an experimental bulk probe of domain-wall physics in the system. In particular, we predict the appearance of an absorption peak due to domain-wall percolation upon tuning the magnetic field across the first-order transition line. We argue that the temperature dependence of this peak could help identify the nature of the phase transition.

DOI: 10.1103/PhysRevResearch.6.023080

I. INTRODUCTION

The realization of multiple superconducting phases is compelling evidence of unconventional superconductivity in a material [1–3]. The observed sequential transitions are often linked to the spontaneous breaking of symmetries within the superconducting phase. Consequently, the phase transitions are of second order, where the order parameters are connected through a group-to-subgroup symmetry relation. In contrast, the recent observation of an additional phase boundary in the H-T-phase diagram of the heavy-fermion superconductor $CeRh_2As_2$ deviates from this pattern. Instead, it seems to align with the characteristics of a first-order transition, marked by a discontinuous change in the order parameter [4,5]. The transition occurs at sufficiently low temperature, when a magnetic field is applied along the c axis of the tetragonal crystal lattice, with the phase boundary remaining essentially temperature independent. The nature of the transition mirrors that of a metamagnetic transition, with a sudden jump in magnetization at a finite magnetic field [6]. This opens the intriguing opportunity to investigate effects originating from the coexistence of the two phases (low and high field), especially in slightly inhomogeneous samples.

$CeRh_2As_2$ has been subject to intense experimental [5,7–18] and theoretical [19–27] investigation in recent years. The most striking features of the H-T phase diagram have been attributed to the staggered noncentrosymmetricity of this compound, where two inequivalent Ce sites (constituting a sublattice degree of freedom) experience different crystal fields from the surrounding Rh and As cages, giving rise to antisymmetric Rashba spin-orbit coupling (ASOC) [27,28]. While inversion symmetry is locally broken at each Ce atom, the point group of the material is D_{4h}, with an inversion center sitting between Ce sites. ASOC induced by local noncentrosymmetricity and the resulting local parity mixing are believed to lend this system a surprising robustness against c-axis magnetic fields, with an extrapolated upper critical field of 14 T despite the low onset temperature of $T_c \approx 0.26$ K to superconductivity [29,30]. The upper critical magnetic field in this case rises in two stages when the temperature is lowered with a kink feature at $T \approx 0.6T_c$ and $H \approx 4$ T, see Fig. 1(a). This anomaly is associated with the first-order phase-boundary line, which separates a low- and a high-field phase and is nearly temperature independent [4].

In this work, we investigate consequences of material inhomogeneity on the properties of the superconductor in the vicinity of the first-order phase boundary in $CeRh_2As_2$. Inhomogeneities give rise to nucleation when the phase boundary is approached upon tuning the magnetic field, with parts of the sample in the low- and others in the high-field phase, A and B, respectively, see Fig. 1(b). In the following, we use the phenomenological Ginzburg-Landau (GL) framework introduced earlier [21] to study the formation and phenomenology of domain walls (DW). As the balance of coexisting regions of A and B can be affected by pressure or strain, we study ultrasound coupling to the DWs, which are shaken and thus provide nonresonant attenuation upon their proliferation in the vicinity of the phase transition.

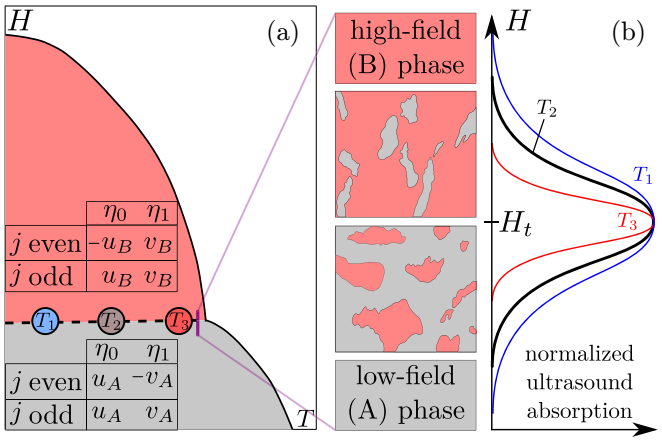

FIG. 1. (a) Schematic phase diagram showing the even-parity low-field A (gray) and odd-parity high-field B (red) superconducting phases separated by a first-order internal phase-transition (dashed) line at $H = H_t$. The inset shows the configuration of the order parameters η_μ^j in layer j with $\mu = 0, (1)$ for even (odd) parity. Here, $u_A > v_A > 0$ and $v_B > u_B > 0$. (b) Schematic depiction of nucleation (left) and evolution of (normalized) absorption peak with temperature (right). Deep in the A or B phase the system is devoid of domain walls. At $H \lesssim H_t$ ($H \gtrsim H_t$) the landscape is dominated by the A (B) phase, with bubbles of B (A). Maximum domain-wall proliferation is expected at $H \approx H_t$. The absorption peak is expected to broaden as temperature is lowered ($T_1 < T_2 < T_3$), which is a distinguishing feature of this first-order phase boundary (see text for details).

II. MODEL

The unit cell of $CeRh_2As_2$ is spanned by two inequivalent layers (or sublattices) stacked in the crystallographic c direction [31] with alternating Rashba-like ASOC. A minimal GL model that reproduces the experimentally observed phase diagram is based on local parity-mixed $(s+p)$-wave pairing and associates the first-order phase boundary with a global parity-switching transition [21,32]. We introduce two layer-dependent order-parameter (OP) components with layer index j, namely, η_0^j, an A_{1g} spin-singlet s-wave OP, and $\boldsymbol{d}_1^j = \eta_1^j[k_y, -k_x, 0]$, the d vector of the odd-parity component, transforming under the A_{2u} representation of the point group D_{4h}. The pertinent GL free-energy density as an expansion in η_0^j and η_1^j is written as

$$
\begin{aligned}
f &= \sum_j \sum_{\mu=0,1} f_\mu^j + f_\epsilon + f_J + f_H, \text{ with} \\
f_\mu^j &= a_\mu \left|\eta_\mu^j\right|^2 + b_\mu \left|\eta_\mu^j\right|^4 + K_\mu \left|\boldsymbol{D}_\parallel \eta_\mu^j\right|^2, \\
f_\epsilon &= \sum_j (-1)^j \epsilon \left(\eta_0^{j*}\eta_1^j + \eta_0^j \eta_1^{j*}\right), \\
f_J &= J \sum_j \sum_\mu \left|\eta_\mu^{j+1} - \eta_\mu^j\right|^2, \\
f_H &= \sum_j \chi H^2 \left|\eta_0^j\right|^2,
\end{aligned}
\tag{1}
$$

where $a_\mu = a_\mu^0 (T - T_{c,\mu})$, with a_μ^0, b_μ, and K_μ positive, real phenomenological constants, and ϵ quantifies the effect of ASOC leading to the coupling between the even- and odd-parity OP and transforms under the A_{2u} representation, whose combination leads to the mixed-parity state mentioned above. Moreover, $\boldsymbol{D}_\parallel = [-i\boldsymbol{\nabla} + 2e\boldsymbol{A}]_\parallel$ is the in-plane covariant derivative. Despite considering the situation in a magnetic field, we do not include the property of the mixed phase and, therefore, omit the vector potential $\boldsymbol{A}$ when discussing the phase diagram. We elaborate on this simplification in Appendix D. The effect of the magnetic field then enters only through the Zeeman coupling to the electron spin, which involves paramagnetic limiting for the even-parity OP with $\sum_j \chi |\eta_0^j|^2$ yielding a reduction of the Pauli spin susceptibility [33]. While we introduced the bare critical temperatures for both OP components, their ASOC-induced coupling yields a slightly higher effective onset of superconductivity, $T_c > T_{c,\mu}$.

In the limit of vanishing interlayer coupling incorporated by the Josephson-like J term, the staggered system consists of independent noncentrosymmetric layers, naturally hosting mixed-parity pairing states. Due to the alternating sign of the ϵ term, the relative sign between the two OP components alternates as well, being "+" for even j and "−" for odd j in our setup. A finite J explicitly restores inversion symmetry, enabling us to label the solutions as even and odd under inversion operation, which exchanges the two layers. Assuming that at zero magnetic field the even-parity OP is dominant ($T_{c,0} > T_{c,1}$), the interlayer coupling stabilizes a configuration, where η_0^j has the same phase in all layers while η_1^j alternates its sign. This corresponds to the low-field A phase: $\eta_0^j = \eta_0^{j'} = u_A$, $-\eta_1^j = \eta_1^{j'} = v_A$, with $u_A > v_A > 0$ and $j = 2n$ (even) and $j' = 2n+1$ (odd). In contrast, in the high-field B phase, η_0^j is suppressed through the paramagnetic limiting effect such that the now-dominant η_1^j has the same phase for all layers with an alternating sign for η_0^j: $-\eta_0^j = \eta_0^{j'} = u_B$, $\eta_1^j = \eta_1^{j'} = v_B$, with $v_B > u_B > 0$, as described, for instance, in Ref. [21]. It is straightforward to show that the transition occurs at a magnetic field given by $H_t = \sqrt{(a_1 - a_0)/\chi}$. The model outlined in Eq. (1) is geared toward capturing the internal phase transition and does not account for orbital depairing that ultimately destroys the B phase at high fields. Nevertheless, the above formula for H_t provides a good approximation even in the presence of the vortex lattice. Indeed, the transition occurs in the mixed phase of a strongly type-II superconductor at a field where the vortex density is rather high and the field practically uniform [21]. Our model coarse grains the order parameter, neglecting the short-range modulations due the vortices with a very small core size (see Appendix D). Because the inversion operation exchanges even and odd layers, we may characterize A as *even*- and B as *odd*-parity phase.

At sufficiently low temperature, both phases correspond to separate minima of the GL free energy, where at $H = H_t$ they exchange their role as the global minimum and give rise to a first-order transition, as can be shown also based on general thermodynamic arguments [34,35]. Importantly, in a spatially inhomogeneous material, we expect the transition to not happen everywhere at the same field H_t, but to show regions of one phase embedded within the other, whereby the OPs rearrange between even and odd configurations on a length

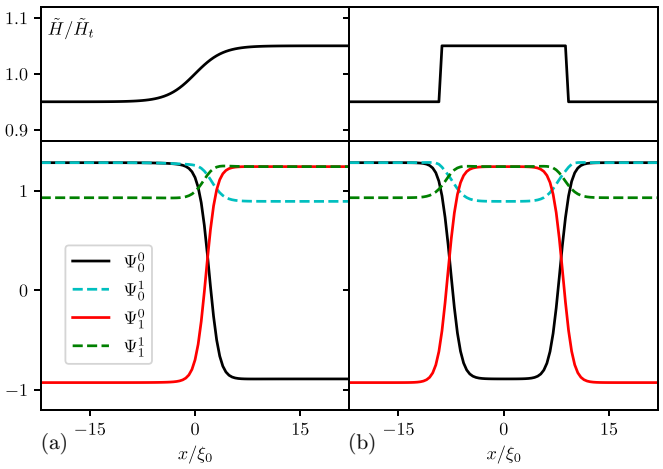

FIG. 2. Effective magnetic field profiles (top row) and the resulting OP configurations (bottom row) computed via numerical minimization. (a) Hyperbolic tangent inhomogeneity with width $4\xi_0$, and (b) a double DW configuration. All $\tilde{H}(x)$ profiles are symmetric with respect to $\tilde{H}_t$ with a maximum deviation of 5%. For the numerical calculations, we fix temperature to $T/T_{c,0} = 0.5$ and use the parametrization $b_\mu = b$, $K_\mu = K$, $-a_0/b = K/|a_0| = 1$, $a_1/a_0 = 0.105$, $J/|a_0| = 1$, and $\epsilon/|a_0| = 2$. Lengths are expressed in units of $\xi_0 = \sqrt{K/|a_0|}$ and the OP as $\Psi_\mu^j = \sqrt{-b/a_0}\eta_\mu^j$.

scale of order coherence length $\xi_0 = \sqrt{K/|a_0|}$, constituting sharp DWs.

III. DOMAIN WALLS

Inhomogeneities in the sample lead to spatially varying parameters and thus, critical field. We incorporate such inhomogeneities in our GL model through a position-dependent parameter $\chi(\boldsymbol{r})$, assuming a relatively slow variation in space, which only enters the Zeeman term f_H in the free energy. In order to investigate the structure of a DW, we restrict ourselves to a one-dimensional spatial dependence $\chi(x)$, use the parametrization $\sqrt{\chi(x)}H \equiv \tilde{H}(x)$, and, for a model calculation, consider a step-like dependence, $\tilde{H}(x) = H_0 + H_1 \tanh(x/\delta)$, with $H_0 - H_1 < \tilde{H}_t < H_0 + H_1$ and $\tilde{H}_t = \sqrt{a_1 - a_0}$ corresponding to the transition point. In this way, the A (B) phase is favored for $x < 0$ ($x > 0$). We minimize the free energy numerically using the one-step relaxed Newton-Jacobi method [36] and obtain a smooth, narrow DW between the two phases, as displayed in Fig. 2(a). Using a profile for $\tilde{H}(x)$ with two opposite steps shows an "island" of B phase inside the A phase [Fig. 2(b)], as it may occur at the verge of the bulk phase transition. The position of the DW is pinned by the specific x dependence of $\tilde{H}(x)$, roughly at the position $\tilde{H}(x_0) = \tilde{H}_t$ [$x_0 = 0$ in Fig. 2(a)]. In what follows, we consider a harmonic pinning potential for the DW position.

Note that, unlike deep in the A or B phase, within the DW the OP does not adhere to global parity classification. We also remark that the deformation of OPs in the vicinity of the DW combined with the local noncentrosymmetricity yields a nonvanishing spin current along the domain boundary [37], see Appendix A. However, we do not dwell on this feature in the following, but rather consider the effects of strain in the system.

IV. ULTRASOUND PROBE

Recent experiments observed a significant effect of hydrostatic pressure on the superconducting phase diagram of $CeRh_2As_2$. Most glaringly, pressure decreases the overall T_c and affects the balance between A and B phases [12,13]. Owing to its tetragonal symmetry, the phase diagram of $CeRh_2As_2$ under hydrostatic pressure can also be appreciated qualitatively by considering that strain along the c axis changes the ratio between the strength of parity mixing and interlayer coupling, namely, ϵ/J. While this aspect may be more purposefully investigated by uniaxial c-axis strain, here we propose a related experiment based on ultrasound modes.

For this purpose, we first discuss the coupling of DWs to ultrasound. DWs represent a boundary between two phases with vortex lattices of different flux density and, thus, different mean magnetization. The first-order nature of the phase transition furthermore yields a jump in magnetization [21], quite analogous to a metamagnetic transition. Naturally, this induces a supercurrent flowing within the layers along the domain boundary. The temporal variation of strain through the ultrasound waves leads to a periodic displacement of the DW and yields a dissipation via the motion of currents as well as the vortices near the DW. Thus, we expect an extra contribution to ultrasound absorption due to local nucleation in the vicinity of the first-order phase boundary.

To formulate this concretely, we introduce an ultrasound mode as a longitudinal plane wave of frequency ω propagating in the z direction (crystallographic c axis), $\boldsymbol{u}(\boldsymbol{r}, t) = \hat{z}u_0 e^{ikz - i\omega t}$, where $\boldsymbol{u}$ is the lattice displacement field and k is the wave vector along z, which depends on the properties of the medium. This mode transforms under the trivial A_{1g} representation and hence is not symmetry breaking. Since the only relevant element in the strain tensor is $\epsilon_{zz} = \partial_z u_z$, we focus in the discussion of the deformation energy and strain-OP coupling on this component only. Then, the corresponding additional terms to the free energy include the elastic energy $f_{\rm el}$ and the coupling term $f_{s\eta}$, yielding [38]

$$f_{\rm el} = \frac{c_{33}}{2}\epsilon_{zz}^2 = \frac{c_{33}}{2}(\partial_z u_z)^2,$$
$$f_{s\eta} = \sum_j \left(\gamma_0 \epsilon_{zz}\left|\eta_0^j\right|^2 + \gamma_1 \epsilon_{zz}\left|\eta_1^j\right|^2\right), \tag{2}$$

with c_{33} the elastic constant and $\gamma_{0,1}$ phenomenological coupling constants. These terms describe the modification of the phase diagram under c-axis uniaxial strain.

The DWs are pinned by the spatial inhomogeneities of $\tilde{H}(x)$, which we model by a harmonic potential around a given equilibrium position. The free-energy densities of the two phases have different pressure dependence, therefore strain imposes a force to shift the DW from its original equilibrium position. If in the absence of strain the DW is at $x = x_0$, we define the shifted coordinate $\bar{x} = (x - x_0)$, and write the DW potential term as

$$f_{\rm DW} = \tfrac{1}{2}c(\tilde{H})\bar{x}^2 + \gamma\epsilon_{zz}\bar{x}. \tag{3}$$

For $\epsilon_{zz} \neq 0$, the minimum is shifted to $\bar{x} = -\gamma\epsilon_{zz}/c(\tilde{H})$, with γ a measure for the coupling of strain and DW. Note that for simplicity, we assume a DW that is infinitely extended in the y- and z direction such that we can model our system in one spatial dimension (x). The coefficient of the quadratic term

$c(\tilde{H})$ depends on the details of $\tilde{H}(x)$, and by linearizing we find to leading order that $c(\tilde{H}) \propto (\partial \tilde{H}(x)/\partial x)|_{x=0}$. Intuitively, a steeper inhomogeneity profile yields a stiffer potential, restricting the DW motion. On the other hand, γ is independent of $\tilde{H}(x)$ and can be approximated through the different strain dependence of energy densities in the A and B phases, f_A and f_B, respectively, such that

$$\gamma \propto \left(\frac{\partial f_A}{\partial \epsilon_{zz}} - \frac{\partial f_B}{\partial \epsilon_{zz}} \right) \Bigg|_{\epsilon_{zz}=0}. \tag{4}$$

Note that the equilibrium position still depends on the details of $\tilde{H}(x)$. For details of the above calculation see Appendix B.

We model nonresonant absorption by the overdamped oscillation of the DW position and write the equation of motion for $\bar{x}$ as well as the displacement field u_z as [38]

$$\eta \partial_t \bar{x} = -\frac{\partial f_{\text{tot}}}{\partial \bar{x}}, \quad \rho \partial_t^2 u_z(\boldsymbol{r}, t) = \sum_i \partial_i \frac{\partial f_{\text{tot}}}{\partial [\partial_i u_z(\boldsymbol{r}, t)]}. \tag{5}$$

Here, $f_{\text{tot}} = f + f_{\text{el}} + f_{s\eta} + f_{\text{DW}}$, η is a phenomenological viscosity constant resulting from the dissipation due to the motion of the DW, and ρ is a mass density. We can solve these equations in Fourier space, where an external drive of frequency ω results in the wave vector

$$k = \frac{\sqrt{\rho}\omega}{\sqrt{c_{33} - \frac{\gamma^2}{i\omega\eta + c}}}. \tag{6}$$

This finally yields the ultrasound absorption coefficient

$$\alpha = -\text{Im}\, k = \frac{\gamma^2}{2c_{33}c_s\eta} \frac{\omega^2}{\omega^2 + \omega_0^2}, \tag{7}$$

where $c_s = \sqrt{c_{33}/\rho}$ denotes the sound velocity and $\omega_0 = c/\eta$ is a characteristic frequency of the DW. For details of the above calculation consult Appendix C. The coefficient α is a measure for the absorption per unit area of the DW. The total absorption is proportional to the spatial average of α, as well as the DW density in the system for a given external magnetic field. Below, we elaborate on the evolution of the latter as one tunes the magnetic field across H_t. As pointed out earlier, larger value of c (steeper inhomogeneity profile) describes stronger pinning, which in turn results in a reduced motion of the DW and, therefore, less absorption, which is reflected in Eq. (7). Hence, c is in general position dependent. The origin of the viscosity parameter η is analogous to that of vortex motion in the mixed phase of a superconductor, but depends on the microscopic details of the DW.

Our simple model accounts for the contribution to ultrasound absorption per unit area of a DW. As such, the total ultrasound absorption depends on the DW density upon driving the external magnetic field through the phase boundary at H_t. As the magnetic field approaches H_t from below, islands of the high-field phase B appear due to inhomogeneities within the A phase, as schematically shown in Fig. 1(b). In our one-dimensional model, such a B-phase bubble is depicted in Fig. 2(b). Upon increasing the field, the islands bounded by a DW proliferate and eventually DWs percolate through the sample. A further rise of the magnetic field leads to the shrinkage of A domains in a landscape dominated by the B phase [see Fig. 1(b)]. Naturally, the largest contribution to sound absorption is expected when the DWs percolate and their density is largest, such that the absorption shows a peak as a function of the external field.

Finally, let us make some practical remarks on the experimental signatures that would help identify the absorption mechanism in a material like $CeRh_2As_2$. To date, the first-order nature of the internal phase transition has not been unambiguously established. Since tuning across a possible second-order phase transition could also yield an absorption peak (analogous to critical opalescence), the observation of an absorption peak alone may not be conclusive. However, if temperature is lowered when the system is on the verge of a second-order phase transition, the critical region narrows with the accompanying absorption peak becoming sharper. In contrast, the superconducting coherence length, given in our model by $\xi_0 = \sqrt{K/|a_0|}$, decreases with decreasing temperature, whereby the OPs can realize a DW on a smaller length scale, thus in a wider magnetic field range. For this reason, a first-order phase transition with accompanying local nucleation tends to broaden the absorption peak as a function of field when the temperature is lowered, as the opposite phase can nucleate more easily on smaller inhomogeneities. The evolution of an absorption peak as a function of temperature may therefore help pin down the order of the internal phase transition in this system.

V. DISCUSSION

While the proposed mechanism of ultrasound absorption provides a way to detect the first-order transition between phases A and B in the presence of sample inhomogeneity or inhomogeneous magnetic field, the nonuniform nucleation could also be observed by other means. The different vortex density in the two phases [21] may be possible to track by surface scanning probes by observing either the magnetic field or the vortex lattice on its own. A further interesting aspect is the different spin susceptibilities of the A and B phases. Nuclear magnetic resonance (NMR) Knight-shift measurements as a local probe would in principle be able to observe two distinct signals with a varying volume fraction of the two domains as the magnetic field is tuned through $H \sim H_t$.

This work was motivated by the heavy fermion superconductor $CeRh_2As_2$. Some aspects of our discussion, however, might not apply straightforwardly to this material. Recent NMR measurements indicate the presence of magnetic order coexisting with the A phase, but not with the B phase [5,16]. We did not attempt here to integrate this feature into our discussion, since it is unclear so far how this material-specific property connects to the field-induced (first-order) transition. An interesting point we also leave open for the time being is the study of the damping mechanism, such as the effect of DW shape and supercurrents on the viscous motion of DWs. Naturally, such questions become more urgent once the presence of DWs is established. Still, besides probing the physics of nucleation in a superconducting context, our efforts may help further understand the phase diagram of $CeRh_2As_2$, where investigations are still in their early stages.

ACKNOWLEDGMENTS

We thank Elena Hassinger, Manuel Brando, Stanislaw Galeski, and Maximilian Holst for useful discussions. A.S.

and M.S. are grateful for financial support from the Swiss National Science Foundation (SNSF) through Division II (No. 184739). M.H.F. also acknowledges financial support from SNSF through Division II (No. 207908).

APPENDIX A: SPIN CURRENT

Analogously to the case of charge currents and U(1) vector potential, to compute spin currents in the GL formalism we construct an SU(2) gauge field $A^a_\mu(\boldsymbol{x})$, where $\mu = x, y$ are spatial indices and $a = x, y, z$ is the SU(2) index [37]. Due to the magnetic field aligned with $\hat{\boldsymbol{z}}$, we can single out the $A^z_\mu(\boldsymbol{x})$ component. The gauge field (an E_u quantity) coupled to the spin S_z (an A_{2g} quantity) transforms as $E_u \otimes A_{2g} = E_u$, and with the appropriate basis vectors this object reads $\{A^z_y, -A^z_x\}$. Then, the symmetry-allowed nonvanishing term in the free energy is of the form

$$f_{\rm sc} = \sum_j \hat{D}_x A^z_y (-1)^j \epsilon \left(\eta^j_0 \eta^{j*}_1 + \text{c.c.}\right),$$

with $\hat{D}_x$ the derivative operator along x. The spin current along y is then $J^y_z = (\partial f_{\rm sc}/\partial_{A^z_y})|_{A^z_y=0}$, yielding two independent contributions localized to the DW (where the derivative is nonvanishing) as

$$J^y_z = \sum_{j=0,1} (-1)^j \epsilon \left[L_1 \frac{\partial \eta^j_0}{\partial x} \eta^{j*}_1 + L_2 \eta^j_0 \frac{\partial \eta^{j*}_1}{\partial x} + \text{c.c.} \right], \quad \text{(A1)}$$

with $L_{1,2}$ phenomenological coefficients.

APPENDIX B: DOMAIN-WALL POTENTIAL

In the main text, we briefly motivate the form of the DW potential term in the free energy as

$$f_{\rm DW} = c(\tilde{H})\bar{x}^2 + \gamma \epsilon_{zz} \bar{x}, \quad \text{(B1)}$$

where $f_{\rm DW}$ and $\bar{x}$ are measured in units of a_0^2/b and ξ_0, respectively, which renders the rest of the parameters dimensionless. We now proceed to elaborate on the coefficients $c(\tilde{H})$ and γ by means of numerical simulations. The stiffness of the quadratic potential is characterized by $c(\tilde{H})$, which depends on the shape of the inhomogeneity through $\tilde{H}(x)$. To leading order, we assume its form to be $c(\tilde{H}) \propto f(w)$ with f some function of $w = (\partial \tilde{H}(x)/\partial x)|_{x=0}$. For $\epsilon_{zz} = 0$, the potential minimum is located at $\bar{x} = 0$, whereas for finite strain it is shifted to

$$\bar{x} = -\frac{\gamma \epsilon_{zz}}{2c(\tilde{H})}. \quad \text{(B2)}$$

For the following analysis, we set the coupling of the order parameters to strain [Eq. (2) of the main text] to $\gamma_0 = \gamma_1 = 0.65$.

To extract the DW potential, we first use the one-step relaxed Newton-Jacobi method [36] to minimize the free energy for $\epsilon_{zz} = 0$ in the presence of a tanh-shaped inhomogeneity, centered around $\tilde{H}_t = \sqrt{a_1 - a_0}$, and with varying width δ. In dimensionless form, the corresponding term in the free energy reads

$$\frac{b}{a_0^2} f_H = \left(\frac{\tilde{H}(x)}{|a_0|}\right)^2 \sum_{j=0,1} \left|\Psi^j_0\right|^2 = (1 - a_1/a_0)[1 + A \tanh(x/\delta)]^2 \sum_{j=0,1} \left|\Psi^j_0\right|^2, \quad \text{(B3)}$$

where in the second equality we measure $\tilde{H}$ in units of $\tilde{H}_t$ and in our analysis we set the maximal deviation $A = 0.05$. The rest of the parameters are the same as in Fig. 2 of the main text. Notice that the above spatial dependence yields $w = A/\delta$. In what follows, we always use a dimensionless free energy and measure any length in units of the coherence length ξ_0.

As a next step, we compute the integral of the free-energy density on $x/\xi_0 \in [-22, 22]$ with the previously derived numerical solution $\Psi^j_\mu(x)$ as a function of an added shift $\int dx f[\Psi^j_\mu(x - \bar{x})]$ in the presence of $-0.1 \leqslant \epsilon_{zz} \leqslant 0$. However, to leading order we use the solution $\Psi^j_\mu(x)$ obtained for zero strain. To proceed and extract $c(\tilde{H})$ and γ, we fit the data obtained this way with a parabola, see Fig. 3. The fit parameters are shown in Table I.

As expected, the coefficient of the quadratic term in the fit is approximately independent of the strain, but varies strongly with δ. Intuitively, the stiffness of the harmonic pinning potential is set by the inhomogeneity profile, in that slower spatial variation (larger δ) yields a softer potential (smaller quadratic coefficient). Therefore, for fixed $\delta/\xi_0 = \{2, 3, 4, 5, 6, 7\}$ we average over ϵ_{zz} and notice that the function $f(w) = pw = pA/\delta$ yields an excellent fit with $p \approx 0.7$, see Fig. 4(a). Hence, we conclude that to leading order $c(\tilde{H}) \propto (\partial \tilde{H}(x)/\partial x)|_{x=0}$.

Introducing $\epsilon_{zz} > 0$ shifts the equilibrium position of the DW by an amount described by Eq. (B2). Here, γ is independent of δ, which can be seen if we shift the linear coefficients in Table I so that for $\epsilon_{zz} = 0$ the fit is purely quadratic ("corr." column). Such a correction is needed because the potential, obtained by shifting a DW solution in the expression of the free energy, is necessarily slightly asymmetric, as the free-energy densities of the two phases on either side of the DW are different, and we integrate them over a finite region.

To extract γ, we average over δ for each ϵ_{zz} and fit the resulting data with a linear function with zero intercept, see Fig. 4(b). This method yields $\gamma \approx 0.094$. Alternatively, γ can be approximated via the change in energy densities of the A and B phases upon varying ϵ_{zz} as in Eq. (4) of the main text. To this end, we minimize the homogeneous free-energy density $f + f_{s\eta}$ in the A and B phases separately (in the absence of DWs) for $\epsilon_{zz} = 0$. Subsequently, as before, we re-evaluate the free-energy densities for varying finite strain, which yields a linear ϵ_{zz} dependence, albeit with different slopes for the A and B phases. The difference in the slopes yields γ. As reproducing this calculation is straightforward, we only quote the result $\gamma \approx 0.109$. The two scenarios therefore yield consistent values for the coupling γ.

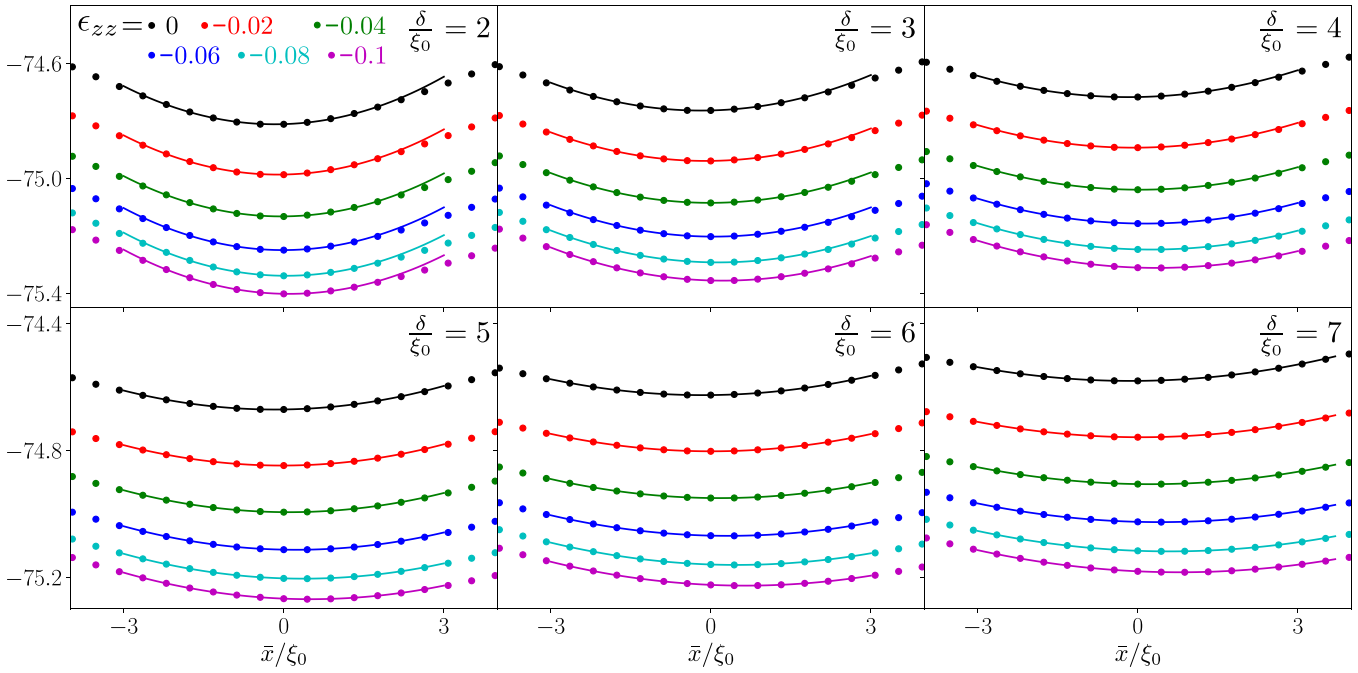

FIG. 3. DW potential (measured in units of b/a_0^2) for various values of ϵ_{zz} and δ, with fitted parabolas for each data set. For clarity we shifted the data sets vertically in the following way: for $\epsilon_{zz} = \{0, -0.02, -0.04, -0.06, -0.08, -0.1\}$ curves are shifted by $(-1) \times \{5, 4, 3, 2, 1\}$ units of free energy, respectively.

APPENDIX C: SOUND ABSORPTION COEFFICIENT

We first consider the equation of motion for the displacement field u_z from Eq. (5) of the main text, yielding

$$\rho \partial_t^2 u_z = \partial_z \left(\sum_{j,\mu} \gamma_\mu \left| \eta_\mu^j \right|^2 + c_{33} \partial_z u_z + \gamma \bar{x} \right). \tag{C1}$$

In the leading-order approximation, we only consider the effect of strain on the DW via coupling to the two phases differently, and not its direct influence on the OPs. Then, we obtain in Fourier space

$$-\rho \omega^2 u_z = -c_{33} k^2 u_z + ik\gamma \bar{x}. \tag{C2}$$

Next, we turn to the equation of motion of $\bar{x}$ in Eq. (5) of the main text and write it as

$$i\omega\eta \bar{x} = -c\bar{x} - ik\gamma u_z, \tag{C3}$$

TABLE I. Fit parameters of the parabolic curves from Fig. 3, with "corr." the corrected linear coefficients, whereby all values for fixed δ are shifted by the same amount such that $\epsilon_{zz} = 0$ yields zero linear coefficient.

	$\delta/\xi_0 = 2$				$\delta/\xi_0 = 3$				$\delta/\xi_0 = 4$			
ϵ_{zz}	Constant	Linear	Corr.	Quadratic	Constant	Linear	Corr.	Quadratic	Constant	Linear	Corr.	Quadratic
0	−69.81	0.0054	0	0.0165	−69.76	0.0044	0	0.0122	−69.72	0.0033	0	0.0093
−0.02	−70.99	0.0035	−0.0020	0.0163	−70.94	0.0022	−0.0022	0.0118	−70.89	0.0013	−0.0019	0.0092
−0.04	−72.13	0.0015	−0.0039	0.0161	−72.09	0.0003	−0.0041	0.0117	−72.04	−0.0007	−0.0039	0.0090
−0.06	−73.25	0.0004	−0.0051	0.0164	−73.20	−0.0013	−0.0057	0.0117	−73.16	−0.0025	−0.0058	0.0088
−0.08	−74.34	−0.0015	−0.0069	0.0162	−74.29	−0.0032	−0.0077	0.0113	−74.25	−0.0043	−0.0076	0.0087
−0.1	−75.40	−0.0032	−0.0087	0.0160	−75.36	−0.0050	−0.0095	0.0111	−75.31	−0.0061	−0.0093	0.0084
	$\delta/\xi_0 = 5$				$\delta/\xi_0 = 6$				$\delta/\xi_0 = 7$			
ϵ_{zz}	Constant	Linear	Corr.	Quadratic	Constant	Linear	Corr.	Quadratic	Constant	Linear	Corr.	Quadratic
0	−69.67	0.0024	0	0.0074	−69.63	0.0018	0	0.0062	−69.58	0.0014	0	0.0053
−0.02	−70.85	0.0004	−0.0020	0.0073	−70.80	−0.0001	−0.0019	0.0061	−70.76	−0.0005	−0.0019	0.0052
−0.04	−72.00	−0.0014	−0.0039	0.0072	−71.95	−0.0020	−0.0038	0.0060	−71.91	−0.0024	−0.0038	0.0051
−0.06	−73.11	−0.0033	−0.0057	0.0071	−73.07	−0.0038	−0.0056	0.0059	−73.03	−0.0042	−0.0056	0.0050
−0.08	−74.20	−0.0051	−0.0075	0.0069	−74.16	−0.0056	−0.0074	0.0058	−74.12	−0.0060	−0.0073	0.0050
−0.1	−75.27	−0.0068	−0.0092	0.0068	−75.22	−0.0073	−0.0091	0.0057	−75.18	−0.0076	−0.0090	0.0049

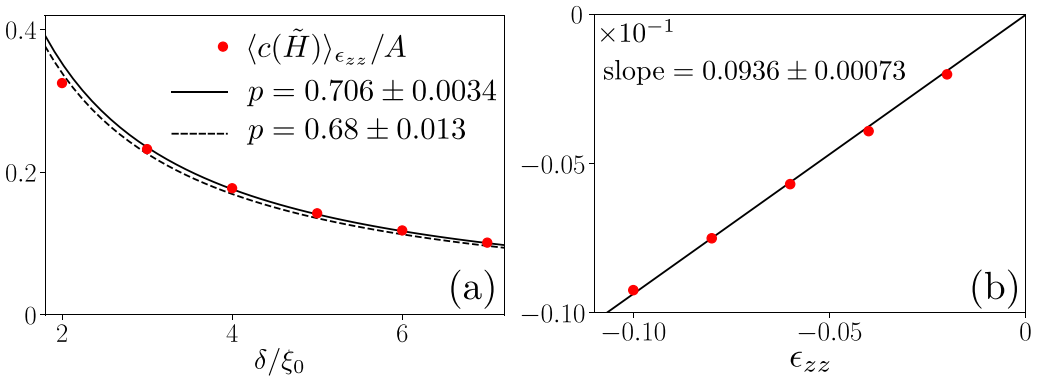

FIG. 4. (a) $c(\tilde{H})/A$ averaged over $\epsilon_{zz} = -k\,0.02$ for $k = 0, 1, \ldots, 5$ (red points) and least square fit of the function p/δ. The dashed line represents a fit of all available data, whereas the solid line ignores the first data point at $\delta = 2\xi_0$, where the inhomogeneity length scale becomes too short and our leading-order approximation is less accurate. (b) Linear coefficients of the parabolic DW potential from Table I, averaged over $\delta/\xi_0 = 2, \ldots, 7$ (red points) and a linear fit with zero intercept (black line).

and eventually we obtain

$$k = \frac{\sqrt{\rho}\omega}{\sqrt{c_{33} - \frac{\gamma^2}{i\omega\eta + c}}} \approx \frac{\sqrt{\rho}\omega}{\sqrt{c_{33}}}\left[1 + \frac{1}{2c_{33}}\frac{\gamma^2}{c + i\omega\eta}\right], \tag{C4}$$

where in the second equality we Taylor expand in $\gamma^2/[c_{33}(c + i\omega\tau)]$. Finally, we arrive at the expression for the absorption coefficient

$$\alpha = -\mathrm{Im}\, k = \frac{\gamma^2}{2c_{33}c_s\eta}\frac{\omega^2}{\omega^2 + \omega_0^2}. \tag{C5}$$

APPENDIX D: VORTEX EFFECTS ON FIRST-ORDER NUCLEATION IN $CeRh_2As_2$

In our treatment of an external magnetic field, we have neglected vortex physics and only incorporated the coupling through a Zeeman term. To estimate the effect of vortices on the first-order nucleation in $CeRh_2As_2$, we first give an approximation to the strength of the self-field, which is roughly equal to H_{c1}. To this end we first estimate the thermodynamic critical field as

$$\mu_0 H_c \approx 10^{-2}\sqrt{\frac{\gamma}{\gamma_0}}T_c[\mathrm{K}] \approx 0.1\ \mathrm{T}, \tag{D1}$$

where $\gamma/\gamma_0 \approx 1000$ in $CeRh_2As_2$ [14], which is the ratio of the Sommerfeld coefficient to that of a normal metal, thus reflecting the heavy-fermion nature of this compound. From here, the Ginzburg-Landau parameter can be estimated as

$$\kappa = \frac{H_{c2}}{\sqrt{2}H_c} \approx 100, \tag{D2}$$

which corresponds to a strongly type-II superconductor. Here, $H_{c2} \approx 14$ T in $CeRh_2As_2$ [4]. Finally, we obtain an approximation of the vortex field using

$$H_{c1} = \frac{H_{c2}}{\kappa^2} \approx 10^{-3}\ \mathrm{T}. \tag{D3}$$

The field of an individual vortex is therefore far too weak to trigger nucleation of the high-field phase, which happens around 4 T.

To address the inhomogeneity due to the vortex lattice close to the first-order line, note that the distance between vortices is on the order $d = \sqrt{\Phi_0/B}$, where Φ_0 is the flux quantum. Around the transition field, this yields $d \approx 10$ nm. On the other hand, the penetration depth λ can be calculated if we first approximate the coherence length from [39]

$$H_{c2} = \frac{\Phi_0}{2\pi\xi^2}, \tag{D4}$$

which yields $\xi \approx 5$ nm, ultimately leading to $\lambda \approx 500$ nm. Since $d \ll \lambda$, for our purposes the field inside the superconductor can be approximated as homogeneous.

[1] R. Joynt and L. Taillefer, The superconducting phases of UPt_3, Rev. Mod. Phys. **74**, 235 (2002).
[2] G. R. Stewart, UBe_{13} and $U_{1-x}Th_xBe_{13}$: Unconventional superconductors, J. Low Temp. Phys. **195**, 1 (2019).
[3] D. Aoki, F. Honda, G. Knebel, D. Braithwaite, A. Nakamura, D. Li, Y. Homma, Y. Shimizu, Y. J. Sato, J.-P. Brison, and J. Flouquet, Multiple superconducting phases and unusual enhancement of the upper critical field in UTe_2, J. Phys. Soc. Jpn. **89**, 053705 (2020).
[4] S. Khim, J. F. Landaeta, J. Banda, N. Bannor, M. Brando, P. M. R. Brydon, D. Hafner, R. Küchler, R. Cardoso-Gil, U. Stockert *et al.*, Field-induced transition within the superconducting state of $CeRh_2As_2$, Science **373**, 1012 (2021).
[5] S. Ogata, S. Kitagawa, K. Kinjo, K. Ishida, M. Brando, E. Hassinger, C. Geibel, and S. Khim, Parity transition of spin-singlet superconductivity using sublattice degrees of freedom, Phys. Rev. Lett. **130**, 166001 (2023).

[6] E. Stryjewski and N. Giordano, Metamagnetism, Adv. Phys. **26**, 487 (1977).

[7] S.-ichi Kimura, J. Sichelschmidt, and S. Khim, Optical study of the electronic structure of locally noncentrosymmetric $CeRh_2As_2$, Phys. Rev. B **104**, 245116 (2021).

[8] J. F. Landaeta, P. Khanenko, D. C. Cavanagh, C. Geibel, S. Khim, S. Mishra, I. Sheikin, P. M. R. Brydon, D. F. Agterberg, M. Brando *et al.*, Field-angle dependence reveals odd-parity superconductivity in $CeRh_2As_2$, Phys. Rev. X **12**, 031001 (2022).

[9] S. Kitagawa, M. Kibune, K. Kinjo, M. Manago, T. Taniguchi, K. Ishida, M. Brando, E. Hassinger, C. Geibel, and S. Khim, Two-dimensional XY-type magnetic properties of locally noncentrosymmetric superconductor $CeRh_2As_2$, J. Phys. Soc. Jpn. **91**, 043702 (2022).

[10] S. Mishra, Y. Liu, E. D. Bauer, F. Ronning, and S. M. Thomas, Anisotropic magnetotransport properties of the heavy-fermion superconductor $CeRh_2As_2$, Phys. Rev. B **106**, L140502 (2022).

[11] S. Onishi, U. Stockert, S. Khim, J. Banda, M. Brando, and E. Hassinger, Low-temperature thermal conductivity of the two-phase superconductor $CeRh_2As_2$, Front. Electron. Mater. **2**, 880579 (2022).

[12] H. Siddiquee, Z. Rehfuss, C. Broyles, and S. Ran, Pressure dependence of superconductivity in $CeRh_2As_2$, Phys. Rev. B **108**, L020504 (2023).

[13] K. Semeniuk, M. Pfeiffer, J. F. Landaeta, M. Nicklas, C. Geibel, M. Brando, S. Khim, and E. Hassinger, Exposing the odd-parity superconductivity in $CeRh_2As_2$ with hydrostatic pressure, arXiv:2312.09729.

[14] K. Semeniuk, D. Hafner, P. Khanenko, T. Lühmann, J. Banda, J. F. Landaeta, C. Geibel, S. Khim, E. Hassinger, and M. Brando, Decoupling multiphase superconductivity from normal state ordering in $CeRh_2As_2$, Phys. Rev. B **107**, L220504 (2023).

[15] D. Hafner, P. Khanenko, E.-O. Eljaouhari, R. Küchler, J. Banda, N. Bannor, T. Lühmann, J. F. Landaeta, S. Mishra, I. Sheikin, E. Hassinger, S. Khim, C. Geibel, G. Zwicknagl, and M. Brando, Possible quadrupole density wave in the superconducting Kondo lattice $CeRh_2As_2$, Phys. Rev. X **12**, 011023 (2022).

[16] M. Kibune, S. Kitagawa, K. Kinjo, S. Ogata, M. Manago, T. Taniguchi, K. Ishida, M. Brando, E. Hassinger, H. Rosner *et al.*, Observation of antiferromagnetic order as odd-parity multipoles inside the superconducting phase in $CeRh_2As_2$, Phys. Rev. Lett. **128**, 057002 (2022).

[17] Y. Wu, Y. Zhang, S. Ju, Y. Hu, Y. Huang, Y. Zhang, H. Zhang, H. Zheng, G. Yang, E.-O. Eljaouhari, B. Song, N. C. Plumb, F. Steglich, M. Shi, G. Zwicknagl, C. Cao, H. Yuan, Y. Liu, Fermi Surface Nesting with Heavy Quasiparticles in the Locally Noncentrosymmetric Superconductor $CeRh_2As_2$, arXiv:2309.06732v2.

[18] X. Chen, L. Wang, J. Ishizuka, K. Nogaki, Y. Cheng, F. Yang, R. Zhang, Z. Chen, F. Zhu, Y. Yanase, B. Lv, and Y. Huang, Coexistence of near-EF flat band and van Hove singularity in a two-phase superconductor, arXiv:2309.05895.

[19] K. Machida, Violation of Pauli-Clogston limit in the heavy-fermion superconductor $CeRh_2As_2$: Duality of itinerant and localized $4f$ electrons, Phys. Rev. B **106**, 184509 (2022).

[20] T. Hazra and P. Coleman, Triplet pairing mechanisms from Hund's-Kondo models: Applications to UTe_2 and $CeRh_2As_2$, Phys. Rev. Lett. **130**, 136002 (2023).

[21] E. G. Schertenleib, M. H. Fischer, and M. Sigrist, Unusual H-T phase diagram of $CeRh_2As_2$: The role of staggered noncentrosymmetricity, Phys. Rev. Res. **3**, 023179 (2021).

[22] K. Nogaki and Y. Yanase, Even-odd parity transition in strongly correlated locally noncentrosymmetric superconductors: Application to $CeRh_2As_2$, Phys. Rev. B **106**, L100504 (2022).

[23] K. Nogaki, A. Daido, J. Ishizuka, and Y. Yanase, Topological crystalline superconductivity in locally noncentrosymmetric $CeRh_2As_2$, Phys. Rev. Res. **3**, L032071 (2021).

[24] D. Möckli and A. Ramires, Two scenarios for superconductivity in $CeRh_2As_2$, Phys. Rev. Res. **3**, 023204 (2021).

[25] A. Ptok, K. J. Kapcia, P. T. Jochym, J. Łażewski, A. M. Oleś, and P. Piekarz, Electronic and dynamical properties of $CeRh_2As_2$: Role of Rh_2As_2 layers and expected orbital order, Phys. Rev. B **104**, L041109 (2021).

[26] D. Möckli and A. Ramires, Superconductivity in disordered locally noncentrosymmetric materials: An application to $CeRh_2As_2$, Phys. Rev. B **104**, 134517 (2021).

[27] D. C. Cavanagh, T. Shishidou, M. Weinert, P. M. R. Brydon, and D. F. Agterberg, Nonsymmorphic symmetry and field-driven odd-parity pairing in $CeRh_2As_2$, Phys. Rev. B **105**, L020505 (2022).

[28] T. Yoshida, M. Sigrist, and Y. Yanase, Topological crystalline superconductivity in locally noncentrosymmetric multilayer superconductors, Phys. Rev. Lett. **115**, 027001 (2015).

[29] M. Sigrist, D. F. Agterberg, M. H. Fischer, J. Goryo, F. Loder, S.-H. Rhim, D. Maruyama, Y. Yanase, T. Yoshida, and S. J. Youn, Superconductors with staggered noncentrosymmetricity, J. Phys. Soc. Jpn. **83**, 061014 (2014).

[30] A. Skurativska, M. Sigrist, and M. H. Fischer, Spin response and topology of a staggered-Rashba superconductor, Phys. Rev. Res. **3**, 033133 (2021).

[31] We use in the following a coordinate system with x and y the in-plane coordinates.

[32] M. H. Fischer, M. Sigrist, D. F. Agterberg, and Y. Yanase, Superconductivity and local inversion-symmetry breaking, Annu. Rev. Condens. Matter Phys. **14**, 153 (2023).

[33] Note that while this first-order correction to the susceptibility cannot capture the low-temperature transition to the normal state, it is sufficient for our discussion of the internal phase transition.

[34] A. J. Leggett, Implications of the ^{3}He phase diagram below 3 mK, Prog. Theor. Phys. **51**, 1275 (1974).

[35] S. K. Yip, T. Li, and P. Kumar, Thermodynamic considerations and the phase diagram of superconducting UPt_3, Phys. Rev. B **43**, 2742 (1991).

[36] W. Törnig, *Eigenwertprobleme und numerische Methoden der Analysis* (Springer, Berlin, Heidelberg, 1979), Vol. 2.

[37] M. F. Holst, M. Sigrist, and M. H. Fischer, Role of topology and symmetry for the edge currents of a two-dimensional superconductor, Phys. Rev. Res. **4**, 013244 (2022).

[38] M. Sigrist, Ehrenfest relations for ultrasound absorption in Sr_2RuO_4, Prog. Theor. Phys. **107**, 917 (2002).

[39] M. Tinkham, *Introduction to Superconductivity* (Courier Corporation, North Chelmsford, 2004).